

## A method for dynamic crack and shear band propagation with phantom nodes

Jeong-Hoon Song<sup>‡,¶</sup>, Pedro M. A. Areias<sup>§,||</sup> and Ted Belytschko<sup>\*,†</sup>

*Theoretical and Applied Mechanics, Northwestern University, Evanston, IL 60208-3111, U.S.A.*

### SUMMARY

A new method for modelling of arbitrary dynamic crack and shear band propagation is presented. We show that by a rearrangement of the extended finite element basis and the nodal degrees of freedom, the discontinuity can be described by superposed elements and phantom nodes. Cracks are treated by adding phantom nodes and superposing elements on the original mesh. Shear bands are treated by adding phantom degrees of freedom. The proposed method simplifies the treatment of element-by-element crack and shear band propagation in explicit methods. A quadrature method for 4-node quadrilaterals is proposed based on a single quadrature point and hourglass control. The proposed method provides consistent history variables because it does not use a subdomain integration scheme for the discontinuous integrand. Numerical examples for dynamic crack and shear band propagation are provided to demonstrate the effectiveness and robustness of the proposed method. Copyright © 2006 John Wiley & Sons, Ltd.

KEY WORDS: extended finite element method; phantom nodes; dynamic fracture; shear band

### 1. INTRODUCTION

We present a new formulation for the modelling of discontinuities that is particularly suited to explicit time integration methods. The formulation enables crack and shear band propagation to be easily treated by low-order elements, particularly with one-point quadrature elements. The method is based on the extended finite element method (XFEM) [1], but it uses a transformation of the nodal variables that leads to the superposed element formalism of the method of Hansbo

---

\*Correspondence to: Ted Belytschko, Theoretical and Applied Mechanics, Northwestern University, 2145 Sheridan Road, Evanston, IL 60208-3111, U.S.A.

†E-mail: tedbelytschko@northwestern.edu

‡E-mail: j-song2@northwestern.edu

§E-mail: p-areias@northwestern.edu

¶Graduate Research Assistant, Northwestern University.

||Post-Doctoral Research Fellow, Northwestern University.

Contract/grant sponsor: Office of the Naval Research; contract/grant number: N0001H-98-1-0578

*Received 28 April 2005*

*Revised 28 December 2005*

*Accepted 28 December 2005*

Copyright © 2006 John Wiley & Sons, Ltd.

and Hansbo [2]. The advantage of this formalism is that the discontinuous element is replaced by two elements with additional phantom nodes or phantom degrees of freedom, so that little modification is needed in existing explicit finite element programs to implement this formulation for elements with cracks or shear bands. The associated shape functions in a cracked or sheared element are identical to the shape functions of an intact element, which leads to certain simplifications of the implementation in existing codes. Within this context, we have also developed simple quadrature rules for the elements with cracks and shear bands that involve only a single quadrature point for each of the superposed elements.

The XFEM was first presented in References [3,4]. The method is an application of the local partition of unity, see References [5,6]. In the case of elements that are completely cracked, the local partition of unity approach in Reference [4] introduces an additional function into the finite element basis, which consists of the product of the element shape functions with the step function. This approach has also been used for the modelling of discontinuities such as cracks in meshless methods [7]. Rabczuk and Belytschko [8] have developed a meshless method called the cracked particle method wherein step functions are introduced in particles that meet a fracture criterion.

Our motivation for introducing another method in view of the plethora of methods that have already been developed is the need for a finite element method that has the simplicity of the cracked particle method of Rabczuk and Belytschko [8] but greater capability in reproducing the actual crack paths than the inter-element fracture methods of Xu and Needleman [9] and Ortiz and Pandolfi [10]. The method is substantially less complex than the dynamic crack propagation methods of Belytschko *et al.* [1]. However, the latter is able to deal with elements that were partially cracked, so that the progression of the crack is modelled more accurately. One of the aims of this paper is to compare the benefits provided by the capability to model partially cracked elements, which this proposed method lacks.

An alternative formulation of dynamic XFEM for elastic fracture has recently been published by Réthoré *et al.* [11]. It uses an XFEM formulation and it is capable of greater accuracy because it employs a time integration scheme which accounts for discontinuities in time. As we will see from the results, the increase in accuracy that accrues to including partially cracked elements in the formulation and implementation is quite marginal for low-order elements; this has also been noted by Areias and Belytschko [12] in three-dimensional static crack propagation studies.

This paper is aimed at developing a highly efficient but nevertheless quite accurate formulation for dynamic fracture and shear band problems based on the XFEM basis functions. As we will show, the method is capable of handling extensive cracking, yet unlike the inter-element crack methods [9,10], it exhibits almost no mesh dependence once the mesh is sufficiently refined to resolve the relevant physics of the problem. For cracks, the approach is similar to that of Hansbo and Hansbo [2]; for shear bands, a new overlaid element formulation is developed. Mergheim *et al.* [13] have recently implemented the Hansbo and Hansbo [2] approach for static crack growth.

In the description of a crack, we make use of implicit functions, i.e. level set theory, to describe the geometry of the cracks, as proposed in References [14,15]. This is not an intrinsic part of the approach, although it does simplify implementations, particularly in three dimensions, which are not considered here.

This paper is organized as follows. In Section 2, we give the displacement fields for modelling elements with discontinuities. In Section 3, we briefly summarize the weak form for

non-linear dynamic analysis and the discretization, with special emphasis on the quadrature rules we have developed for low-order elements. Section 4 presents the constitutive models which are used in this study and finally in Section 5, we give our numerical studies including comparisons with other methods.

## 2. ENRICHED DISPLACEMENT FIELDS FOR DISCONTINUITY

Consider an initial domain  $\Omega_0$  as shown in Figure 1. The motion is described by  $\mathbf{x} = \phi(\mathbf{X}, t)$  where  $\mathbf{X}$  and  $\mathbf{x}$  denote material and spatial co-ordinates, respectively. In the current domain, the image of the initial domain  $\Omega_0$  is denoted by  $\Omega$ . We allow this domain to contain discontinuities such as cracks and shear bands.

Each discontinuous surface is implicitly defined by the signed distance function  $f(\mathbf{X})$  so that  $f(\mathbf{X}) = 0$  gives the discontinuity surface. This implicit definition can be described in terms of the shape functions and is then given by

$$\sum_I f_I N_I(\mathbf{X}) = 0 \quad (1)$$

We also define a function  $g(\mathbf{X}, t)$  so that the discontinuity is contained within the subdomain  $g(\mathbf{X}, t) > 0$ . Thus, the discontinuity is defined by

$$\mathbf{X} \in \Gamma_c^0 \quad \text{if } f(\mathbf{X}) = 0 \text{ and } g(\mathbf{X}, t) > 0 \quad (2)$$

Note that the implicit functions  $f(\mathbf{X})$  and  $g(\mathbf{X}, t)$  need only to be defined locally around the discontinuity. Furthermore, for elementwise propagation of the discontinuity, we can replace the function  $g(\mathbf{X}, t)$  by the index set of those elements that are cracked or sheared (Figure 2).

### 2.1. Representation of a discontinuity with phantom nodes

In the following, we will refer specifically to a crack, although the arguments also apply to a shear band. We first illustrate the crack modelling concept in one dimension. Consider a crack at  $X = a$  and let the nodes of the element containing the crack be nodes 1 and 2 as shown in

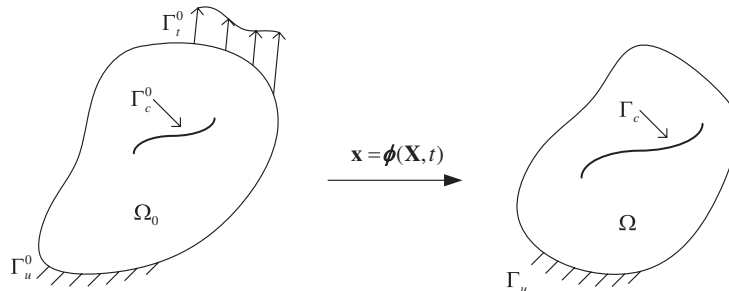


Figure 1. A two-dimensional body with a discontinuity and its representation in the initial and the current domains.

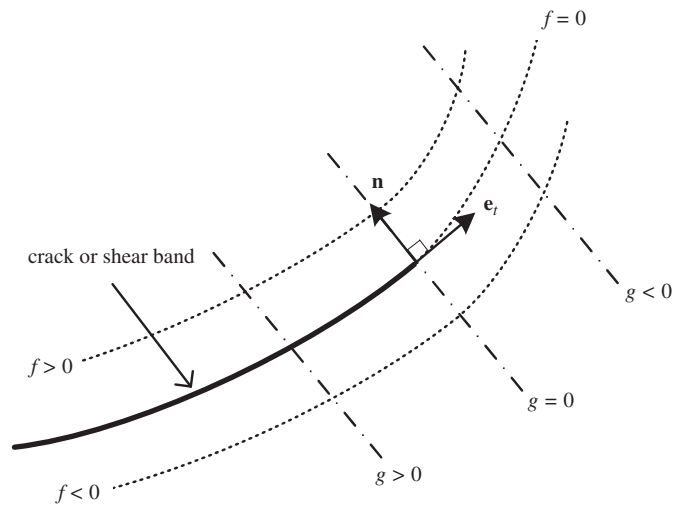


Figure 2. A two-dimensional discontinuity representation by two implicit functions  $f(\mathbf{X})$  and  $g(\mathbf{X}, t)$ .

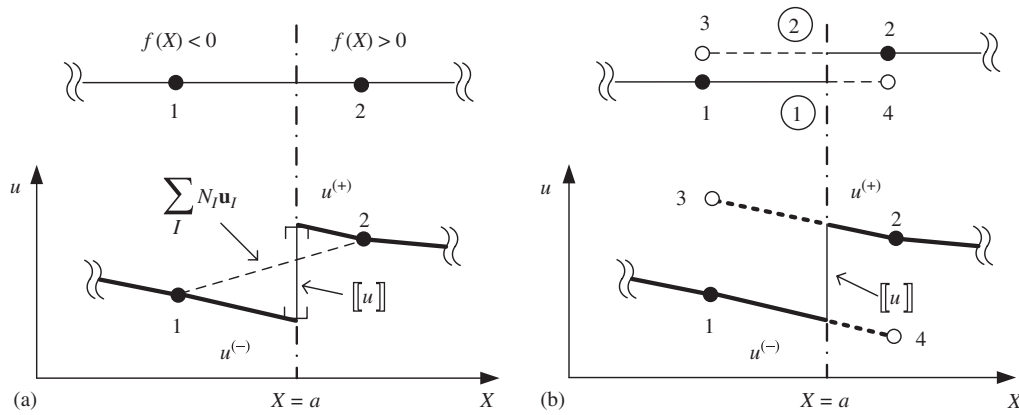


Figure 3. The representation of a discontinuity in a one-dimensional model for: (a) standard XFEM; and (b) phantom node method; solid circles denote real nodes and hollow circles denote phantom nodes.

Figure 3(a). We start with the standard XFEM description of the discontinuous displacement field in an element

$$\mathbf{u}(X, t) = \sum_{I=1}^2 N_I(X) \{ \mathbf{u}_I(t) + \mathbf{q}_I [H(X - a) - H(X_I - a)] \} \quad (3)$$

where  $H(x)$  is the Heaviside step function given by

$$H(x) = \begin{cases} 1 & x > 0 \\ 0 & x \leq 0 \end{cases} \quad (4)$$

We will now transform this to a superposed element formulation for the specific case where node 1 is to the left of the discontinuity as shown in Figure 3(b); the general transformation is given subsequently. Writing out Equation (3) in abbreviated notation, we have

$$u = u_1 N_1 + u_2 N_2 + q_1 N_1 H + q_2 N_2 (H - 1) \quad (5)$$

where  $H = H(X - a)$ . We can rewrite the above equation as

$$u = (u_1 + q_1) N_1 H + u_1 N_1 (1 - H) + (u_2 - q_2) N_2 (1 - H) + u_2 N_2 H \quad (6)$$

where we have used the identities  $N_1 = N_1 H + N_1 (1 - H)$  and  $N_2 = N_2 H + N_2 (1 - H)$ . We now define

$$\text{element 1} \quad \begin{cases} u_1^1 = u_1 \\ u_2^1 = u_2 - q_2 \end{cases} \quad (7)$$

$$\text{element 2} \quad \begin{cases} u_1^2 = u_1 + q_1 \\ u_2^2 = u_2 \end{cases} \quad (8)$$

where superscripts and subscripts denote the element and node numbers, respectively. Equation (6) can then be rewritten as

$$u = u_1^1 N_1 (1 - H(X - a)) + u_2^1 N_2 (1 - H(X - a)) + u_1^2 N_1 H(X - a) + u_2^2 N_2 H(X - a) \quad (9)$$

Thus, we can consider the displacement field to consist of the displacement fields of two elements: element 1, which is only active for  $X < a$ , because of the terms  $(1 - H(X - a))$  and element 2, which is only active for  $X > a$  because of the terms  $H(X - a)$ . The displacement jump across the crack is

$$\begin{aligned} \llbracket u \rrbracket_{X=a} &= \lim_{\varepsilon \rightarrow 0} [u(X + \varepsilon) - u(X - \varepsilon)]_{X=a} \\ &= N_1(a)(u_1^2 - u_1^1) + N_2(a)(u_2^2 - u_2^1) \\ &= q_1 N_1(a) + q_2 N_2(a) \end{aligned} \quad (10)$$

From Equation (9), we can see that the discontinuous field can be constructed by adding an extra element, element 2 in this case, as shown in Figure 3(b). Then two phantom nodes are added: in this case they are  $u_2^1$  and  $u_1^2$ . As shown in Figure 3(b), the two parts of the model are completely disjoint except for a cohesive law which relates the traction across the discontinuity to the jump in the displacement.

For a multi-node element in two or three dimensions that is completely cut by a crack as defined by Equation (2), the two-element displacement field form can be developed similarly. We start with the conventional XFEM displacement field

$$\mathbf{u}(\mathbf{X}, t) = \sum_{I=1}^{n^N} N_I(\mathbf{X}) \{ \mathbf{u}_I(t) + \mathbf{q}_I [H(f(\mathbf{X})) - H(f(\mathbf{X}_I))] \} \quad (11)$$

Expanding the above as we did for the one-dimensional case by subdividing each term into parts that are associated with  $f(\mathbf{X}) < 0$  and  $f(\mathbf{X}) > 0$ , we have

$$\mathbf{u} = \sum_{I=1}^{n^N} [\mathbf{u}_I N_I (1 - H) + \mathbf{u}_I N_I H + \mathbf{q}_I (H - H_I) N_I] \quad (12)$$

where  $H = H(f(\mathbf{X}))$ . We now further expand both fields by duplicating them with the multipliers  $H_I^- = H(-f(\mathbf{X}_I))$  and  $H_I^+ = H(f(\mathbf{X}_I))$ , which does not change the fields and make use of the fact that  $H - H_I = H - 1$  when  $H_I^+ \neq 0$  and  $H - H_I = H$  when  $H_I^- \neq 0$ :

$$\begin{aligned} \mathbf{u} = \sum_{I=1}^{n^N} & [\mathbf{u}_I H_I^+ N_I (1 - H) + \mathbf{u}_I H_I^- N_I (1 - H) + \mathbf{u}_I H_I^+ N_I H + \mathbf{u}_I H_I^- N_I H \\ & + \mathbf{q}_I H_I^+ N_I (H - 1) + \mathbf{q}_I H_I^- N_I H] \end{aligned} \quad (13)$$

We then rewrite the above as

$$\begin{aligned} \mathbf{u} = \sum_{I=1}^{n^N} & [(\mathbf{u}_I - \mathbf{q}_I) H_I^+ N_I (1 - H) + \mathbf{u}_I H_I^- N_I (1 - H) \\ & + \mathbf{u}_I H_I^+ N_I H + (\mathbf{u}_I + \mathbf{q}_I) H_I^- N_I H] \end{aligned} \quad (14)$$

If we then let

$$\mathbf{u}_I^1 = \begin{cases} \mathbf{u}_I & \text{if } f(\mathbf{X}_I) < 0 \\ \mathbf{u}_I - \mathbf{q}_I & \text{if } f(\mathbf{X}_I) > 0 \end{cases} \quad (15)$$

$$\mathbf{u}_I^2 = \begin{cases} \mathbf{u}_I + \mathbf{q}_I & \text{if } f(\mathbf{X}_I) < 0 \\ \mathbf{u}_I & \text{if } f(\mathbf{X}_I) > 0 \end{cases} \quad (16)$$

then we can write the displacement field as

$$\mathbf{u}(\mathbf{X}, t) = \sum_{I \in S_1} \underbrace{\mathbf{u}_I^1(t) N_I(\mathbf{X})}_{\mathbf{u}^1(\mathbf{X}, t)} H(-f(\mathbf{X})) + \sum_{I \in S_2} \underbrace{\mathbf{u}_I^2(t) N_I(\mathbf{X})}_{\mathbf{u}^2(\mathbf{X}, t)} H(f(\mathbf{X})) \quad (17)$$

where  $S_1$  and  $S_2$  are the index sets of the nodes of superposed element 1 and 2, respectively. As can be seen from Figure 4, each element contains original real nodes and phantom nodes.

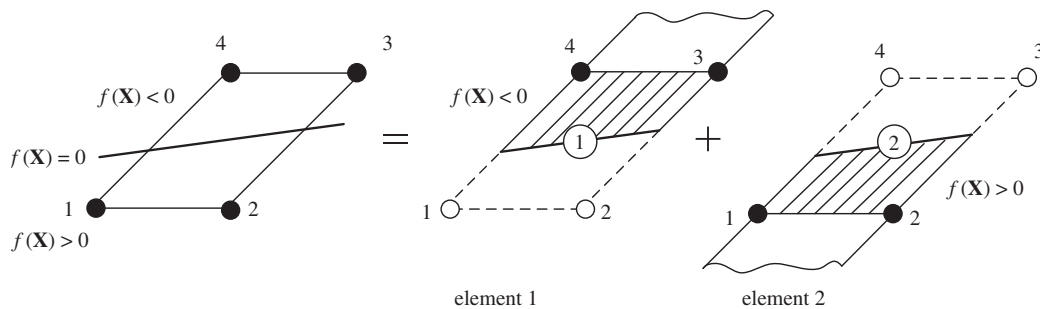


Figure 4. The decomposition of a cracked element with generic nodes 1–4 into two elements; solid and hollow circles denote the original nodes and the added *phantom* nodes, respectively.

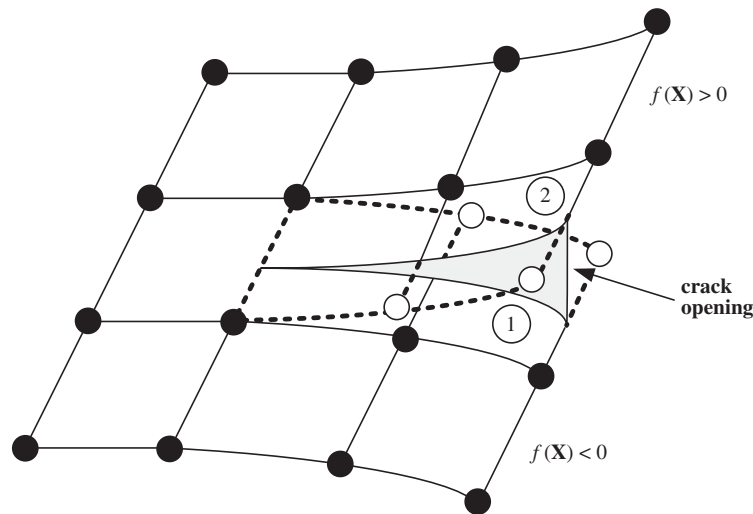


Figure 5. The representation of crack opening with the phantom nodes method; solid and hollow circles denote the original nodes and the added phantom nodes, respectively.

Thus, the XFEM field for a completely cut element can be written as the sum of two element fields; one,  $\mathbf{u}^1(\mathbf{X}, t)$ , which holds for  $f(\mathbf{X}) < 0$  and the other,  $\mathbf{u}^2(\mathbf{X}, t)$ , which holds for  $f(\mathbf{X}) > 0$ . This form corresponds to the concept proposed by Hansbo and Hansbo [2], though they did not present it in this form. It was previously pointed out by Areias and Belytschko [16] that the Hansbo and Hansbo [2] formulation is another form of the XFEM displacement field.

Note that this equivalence holds for any element, i.e. 3-node triangles, 8-node quadrilaterals, etc. Recasting the discontinuous field in this form simplifies the implementation of the element in existing finite element codes. It is only necessary to add an extra element (i.e. element 2 in this case) and phantom nodes and modify the element quadrature procedure (Figure 5). The

phantom nodes are defined by

$$I \text{ is a phantom node in } \begin{cases} \text{element 1} & \text{if } f(\mathbf{X}_I) > 0 \\ \text{element 2} & \text{if } f(\mathbf{X}_I) < 0 \end{cases} \quad (18)$$

All nodes are integrated in time by the same procedure, as will become clear subsequently.

## 2.2. Representation of a shear band with phantom nodes

The same procedure can be used to model shear bands by adding discontinuities in the tangential component of the displacement in elements crossed by a shear band. Let the tangential direction be denoted by  $\mathbf{e}_t$ ; in the context of the level set formulation described here

$$\mathbf{e}_t = \frac{\partial g}{\partial \mathbf{X}} = \nabla_0 g \quad (19)$$

where  $g(\mathbf{X}, t)$  is a signed distance function. The standard XFEM field for a shear band is then

$$\mathbf{u}(\mathbf{X}, t) = \sum_{I=1}^{n^N} N_I(\mathbf{X}) \{ \mathbf{u}_I(t) + \mathbf{q}_I \mathbf{e}_t [H(f(\mathbf{X})) - H(f(\mathbf{X}_I))] \} \quad (20)$$

To develop the shear band element, it is necessary to express the nodal displacements in normal and tangential components, as

$$\mathbf{u}(\mathbf{X}, t) = \sum_{I=1}^{n^N} N_I(\mathbf{X}) \{ \mathbf{u}_{nI}(t) \mathbf{e}_n + \mathbf{u}_{tI}(t) \mathbf{e}_t + \mathbf{q}_I \mathbf{e}_t [H(f(\mathbf{X})) - H(f(\mathbf{X}_I))] \} \quad (21)$$

where  $\mathbf{u}_{nI}(t)$  and  $\mathbf{u}_{tI}(t)$  are the normal and tangential components and  $\mathbf{e}_n$  is the unit normal to the shear band. Going through the same procedure as before, we obtain

$$\begin{aligned} \mathbf{u} &= \sum_{I=1}^{n^N} \mathbf{e}_t [(\mathbf{u}_{tI} - \mathbf{q}_I) H_I^+ N_I (1 - H) + \mathbf{u}_{tI} H_I^- N_I (1 - H) \\ &\quad + \mathbf{u}_{tI} H_I^+ N_I H + (\mathbf{u}_{tI} + \mathbf{q}_I) H_I^- N_I H] + \sum_{I=1}^{n^N} \mathbf{e}_n [\mathbf{u}_{nI} N_I (1 - H) + \mathbf{u}_{nI} N_I H] \\ &= \sum_{I=1}^{n^N} \{ \mathbf{e}_t [(\mathbf{u}_{tI} - \mathbf{q}_I) H_I^+ + \mathbf{u}_{tI} H_I^-] + \mathbf{e}_n \mathbf{u}_{nI} \} N_I H(-f(\mathbf{X})) \\ &\quad + \sum_{I=1}^{n^N} \{ \mathbf{e}_t [(\mathbf{u}_{tI}) H_I^+ + (\mathbf{u}_{tI} + \mathbf{q}_I) H_I^-] + \mathbf{e}_n \mathbf{u}_{nI} \} N_I H(f(\mathbf{X})) \end{aligned} \quad (22)$$

We let

$$\mathbf{u}_{tI}^1 = \mathbf{u}_{tI} - \mathbf{q}_I H(f(\mathbf{X}_I)) \quad (23)$$

$$\mathbf{u}_{tI}^2 = \mathbf{u}_{tI} + \mathbf{q}_I H(f(\mathbf{X}_I)) \quad (24)$$

$$\mathbf{u}_{nI}^1 = \mathbf{u}_{nI}^2 = \mathbf{u}_{nI} \quad (25)$$

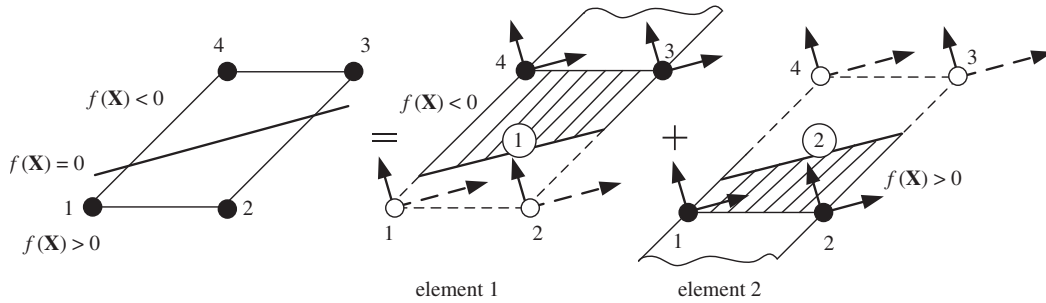


Figure 6. The decomposition of a shear element with generic nodes 1–4; dashed lines indicate phantom degrees of freedom.

Then we can write the displacement field  $\mathbf{u}(\mathbf{X}, t)$  as the sum of two-element displacement fields

$$\mathbf{u}(\mathbf{X}, t) = \mathbf{u}^1(\mathbf{X}, t) + \mathbf{u}^2(\mathbf{X}, t) \tag{26}$$

$$\mathbf{u}^1(\mathbf{X}, t) = \sum_{I \in S_1} \mathbf{u}_{tI} N_I H(-f(\mathbf{X})) + \sum_{I=1}^{n^N} \mathbf{u}_{nI} N_I H(-f(\mathbf{X})) \tag{27}$$

$$\mathbf{u}^2(\mathbf{X}, t) = \sum_{I \in S_2} \mathbf{u}_{tI} N_I H(f(\mathbf{X})) + \sum_{I=1}^{n^N} \mathbf{u}_{nI} N_I H(f(\mathbf{X})) \tag{28}$$

In the shear band elements, phantom degrees of freedom are added only in the tangential direction; the normal components of the nodal displacements correspond to the normal components of the original nodes and are the same in both elements. Consequently, the normal displacement field is also identical in the two elements. The procedure is illustrated in Figure 6, where the phantom degrees of freedom are indicated by dashed lines. The interpretation and its implementation is now somewhat different than for a crack. The construct in Figure 4 is replaced by that shown in Figure 6 and Equations (26)–(28). However, as indicated in Reference [15], the modelling of discontinuous tangential fields where the discontinuity is not rectilinear does present certain difficulties. Some of these difficulties arise because we have used  $C^0$  shape functions to describe the discontinuity surface via Equation (1).

### 3. WEAK FORMULATION AND DISCRETIZATION

#### 3.1. Strong form and weak form

We consider a two-dimensional dynamic problem. The strong form of the linear momentum equation in a total Lagrangian description is

$$\frac{\partial P_{ji}}{\partial X_j} + \rho_0 b_i - \rho_0 \ddot{u}_i = 0 \quad \text{in } \Omega_0 \tag{29}$$

where  $\mathbf{P}$  is the nominal stress tensor,  $\rho_0$  is the initial mass density,  $\mathbf{b}$  is the body force vector.

The boundary conditions are

$$n_j^0 P_{ji} = \bar{t}_i^0 \quad \text{on } \Gamma_t^0 \quad (30)$$

$$u_i = \bar{u}_i \quad \text{on } \Gamma_u^0 \quad (31)$$

$$n_j^0 P_{ji}^- = -n_j^0 P_{ji}^+ = \tau_i^{0c} (\llbracket u_i \rrbracket) \quad \text{on } \Gamma_c^0 \quad (32)$$

where  $\mathbf{n}^0$  is the normal to the indicated boundary,  $\tau^{0c}$  is the cohesive traction across the crack,  $\bar{\mathbf{t}}^0$  is the applied traction on the Neumann boundary  $\Gamma_t$  and  $\bar{\mathbf{u}}$  is the applied displacement on the Dirichlet boundary  $\Gamma_u$ ;  $\Gamma_u^0 \cup \Gamma_t^0 = \Gamma^0$ ,  $\Gamma_u \cap \Gamma_t = \emptyset$ . Superscript plus and minus signs refer to the two sides of the discontinuity. Indicical notation is used for any lower case indices and repeated subscripts imply summations.

The discrete equations are constructed by the standard Galerkin procedures. The admissible space for the displacement fields is defined as follows:

$$\mathcal{U} = \{\mathbf{u}(\mathbf{X}, t) \mid \mathbf{u}(\mathbf{X}, t) \in C^0, \mathbf{u}(\mathbf{X}, t) = \bar{\mathbf{u}}(t) \text{ on } \Gamma_u^0, \mathbf{u} \text{ discontinuous on } \Gamma_c\}$$

$$\mathcal{U}_0 = \{\delta\mathbf{u}(\mathbf{X}, t) \mid \delta\mathbf{u}(\mathbf{X}, t) \in C^0, \delta\mathbf{u}(\mathbf{X}, t) = 0 \text{ on } \Gamma_u^0, \delta\mathbf{u} \text{ discontinuous on } \Gamma_c\}$$

The weak form of the momentum equation is given by: for  $\mathbf{u}(\mathbf{X}, t) \in \mathcal{U}$

$$\delta W^{\text{kin}} = \delta W^{\text{int}} - \delta W^{\text{ext}} + \delta W^{\text{coh}} \quad \forall \delta\mathbf{u}(\mathbf{X}) \in \mathcal{U}_0 \quad (33)$$

where  $\delta W^{\text{int}}$  is the internal work,  $\delta W^{\text{ext}}$  is the external work performed by applied loads,  $\delta W^{\text{kin}}$  is the kinetic work performed by inertia and  $\delta W^{\text{coh}}$  is the work performed by the cohesive traction on the crack surface  $\Gamma_c$ . These quantities are defined as (see Reference [17] for details)

$$\delta W^{\text{kin}} = \int_{\Omega_0} \delta\mathbf{u} \cdot \rho_0 \ddot{\mathbf{u}} \, d\Omega_0 \quad (34)$$

$$\delta W^{\text{int}} = \int_{\Omega_0} \frac{\partial \delta\mathbf{u}}{\partial \mathbf{X}} : \mathbf{P} \, d\Omega_0 \quad (35)$$

$$\delta W^{\text{ext}} = \int_{\Omega_0} \delta\mathbf{u} \cdot \rho_0 \mathbf{b} \, d\Omega_0 + \int_{\Gamma_t^0} \delta\mathbf{u} \cdot \bar{\mathbf{t}}^0 \, d\Gamma_t^0 \quad (36)$$

$$\delta W^{\text{coh}} = - \int_{\Gamma_c} \delta \llbracket \mathbf{u} \rrbracket \cdot \boldsymbol{\tau}^c \, d\Gamma_c \quad (37)$$

where  $\bar{\mathbf{t}}$  is the normalized traction prescribed on  $\Gamma_t^0$  and  $\boldsymbol{\tau}^c$  is the cohesive traction applied on the discontinuity surface; an updated Lagrangian form is used for (37).

The finite element discretization of Equation (33) yields the discrete form of the momentum equation, which leads to

$$\mathbf{f}^{\text{kin}} = \mathbf{f}^{\text{int}} - \mathbf{f}^{\text{ext}} + \mathbf{f}^{\text{coh}} \quad (38)$$

where the internal force  $\mathbf{f}^{\text{int}}$ , the external force  $\mathbf{f}^{\text{ext}}$ , and the cohesive force  $\mathbf{f}^{\text{coh}}$  are assembled from element matrices given below. Since the element matrices are standard, we give them only for a generic pair of elements 1 and 2 crossed by a crack:

$$\mathbf{f}_e^{\text{kin}} = \int_{\Omega_0^e} \rho_0 \mathbf{N}^T \mathbf{N} H((-1)^e f(\mathbf{X})) \, d\Omega_0^e \ddot{\mathbf{u}}_e \tag{39}$$

$$\mathbf{f}_e^{\text{int}} = \int_{\Omega_0^e} \mathbf{B}^T \mathbf{P}_e H((-1)^e f(\mathbf{X})) \, d\Omega_0^e \tag{40}$$

$$\mathbf{f}_e^{\text{ext}} = \int_{\Omega_0^e} \rho_0 \mathbf{N}^T \mathbf{b} H((-1)^e f(\mathbf{X})) \, d\Omega_0^e + \int_{\Gamma_t^{e0}} \mathbf{N}^T \bar{\mathbf{t}}^0 H((-1)^e f(\mathbf{X})) \, d\Gamma_t^{e0} \tag{41}$$

$$\mathbf{f}_e^{\text{coh}} = (-1)^e \int_{\Gamma_c^{e0}} \mathbf{N}^T \tau^c \mathbf{n}_0 \, d\Gamma_c^{e0} \tag{42}$$

where the subscript  $e$  is either 1 or 2 as shown in Figure 4 and the superscript  $e$  indicates a domain restriction to element  $e$ ;  $\mathbf{B}$  is the discrete strain-displacement operator.

### 3.2. One-point integration scheme with hourglass mode control

For evaluation of the integrals Equations (39)–(41) in the elements in which the Heaviside function appears, a modified numerical quadrature scheme such as subdomain integration is needed [1]. In subdomain integration, the element is subdivided into several subdomains, and each subdomain is integrated separately as shown in Figure 7(a). However, several difficulties arise in subdomain integration methods when we consider moving discontinuities. For example, in crack or shear band growth in non-linear materials, the historical variables stored at current quadrature points need to be projected to the newly created quadrature points when a subdomain integration scheme is used.

Here we adopt a one-point integration scheme in which the Gauss quadrature point is fixed. The element uses hourglass mode control; for details on the hourglass mode control scheme, see References [18, 19]. We assume that the stresses are constant within the element and given by the values at the origin of the parent co-ordinate system.

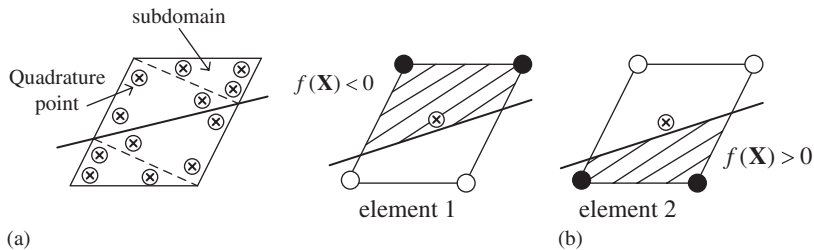


Figure 7. (a) Numerical integration with the subdomain integration scheme; and (b) numerical integration with a one-point integration scheme; hollow circles are the added phantom nodes and solid circles are the original nodes.

As we can see Figure 7(b), the cracked element is replaced by two elements and the nodal forces can be integrated separately as follows:

$$\mathbf{f}_e = \mathbf{f}_{e1} + \mathbf{f}_{e2} \quad (43)$$

where  $\mathbf{f}_e$  is element force matrix of cracked element and  $\mathbf{f}_{e1}$  and  $\mathbf{f}_{e2}$  are the force matrices of newly superposed elements with phantom nodes. Expanding Equations (39)–(42) yields

$$\mathbf{f}_{(e1/e2)}^{\text{kin}} = \frac{A_{(e1/e2)}}{A_0} \int_{\Omega_0^e} \rho_0 \mathbf{N}^T \mathbf{N} d\Omega_0^e \ddot{\mathbf{u}}_{(e1/e2)} \quad (44)$$

$$\mathbf{f}_{(e1/e2)}^{\text{int}} = \frac{A_{(e1/e2)}}{A_0} \int_{\Omega_0^e} \{\mathbf{B}^T \mathbf{P}_{(e1/e2)} + \mathbf{f}_{(e1/e2)}^{\text{stab}}\} d\Omega_0^e \quad (45)$$

$$\mathbf{f}_{e1}^{\text{ext}} = \frac{A_{e1}}{A_0} \int_{\Omega_0^e} \rho_0 \mathbf{N}^T \mathbf{b} d\Omega_0^e + \int_{\Gamma_t^{e0}} H(-f) \mathbf{N}^T \bar{\mathbf{t}}^0 d\Gamma_t^{e0} \quad (46)$$

$$\mathbf{f}_{e2}^{\text{ext}} = \frac{A_{e2}}{A_0} \int_{\Omega_0^e} \rho_0 \mathbf{N}^T \mathbf{b} d\Omega_0^e + \int_{\Gamma_t^{e0}} H(f) \mathbf{N}^T \bar{\mathbf{t}}^0 d\Gamma_t^{e0} \quad (47)$$

$$\mathbf{f}_{e1}^{\text{coh}} = - \int_{\Gamma_c^{e0}} \mathbf{N}^T \tau^c \mathbf{n}_0 d\Gamma_c^{e0} \quad (48)$$

$$\mathbf{f}_{e2}^{\text{coh}} = \int_{\Gamma_c^{e0}} \mathbf{N}^T \tau^c \mathbf{n}_0 d\Gamma_c^{e0} \quad (49)$$

where  $\mathbf{f}^{\text{stab}}$  is a stabilization force matrix to control the hourglass modes,  $A_0$  is the total area of the uncracked element and  $A_{e1}$  and  $A_{e2}$  are the activated areas of the corresponding superposed elements, which consist of regular and phantom nodes. As we can see from Equations (44)–(47), when we compute the force matrix for a cracked element we only modify it by the area fraction. This computational procedure can be easily implemented within the context of the conventional software; it can also be applied to elements with full quadrature.

### 3.3. Time integration scheme and critical time step

In this study, explicit time integration is used over the whole domain. By studying the eigenvalues  $\lambda_i$  of the one-dimensional discrete system  $\lambda_i^2 \mathbf{M} \mathbf{d}_i = \mathbf{K} \mathbf{d}_i$ , we determined the variation of the critical time step size according to the location of the discontinuity. In Figure 8, we can see that the critical time step has a peak value when the discontinuity is at the centre of the element; it drops to zero linearly as the discontinuity is moved to the element edge. To prevent numerical difficulties in the explicit time integration scheme due to zero critical time step, we add small amount of artificial mass to the cracked elements. The eigenvalues are same as for

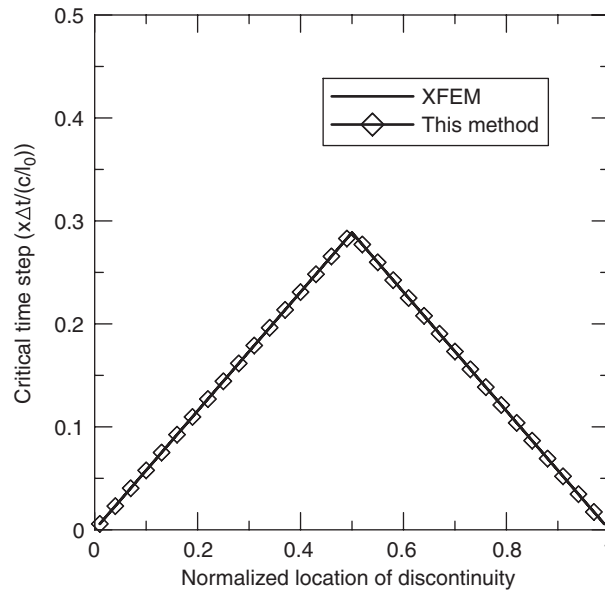


Figure 8. The variation of critical time step size according to the location of the normalized discontinuity.

the conventional XFEM [1], this is not surprising since the displacement field basis is a linear combination of the XFEM basis.

#### 4. CONSTITUTIVE MODEL

##### 4.1. Cohesive law

A cohesive crack model is used for the crack and shear band. In this model, a surface traction is applied onto the surface  $\Gamma_c$ . The cohesive traction is determined by a cohesive law which relates the traction to the jump in displacement across the discontinuity surface. The cohesive laws used in this study are shown in Figure 9.

The cohesive law is constructed so that the energy dissipated due to the crack propagation matches the critical fracture energy. For example, for the linear cohesive model in Figure 9, we have

$$\delta_{\max} = \frac{2G_F}{\tau_{\max}} \quad (50)$$

In this work, we considered only the normal component of the cohesive traction.

##### 4.2. Damage model

One of the material laws used here is the damage model of Lemaitre [20]. In this model, the scalar damage parameter  $D$  represents the extent of damage. This constitutive model was only

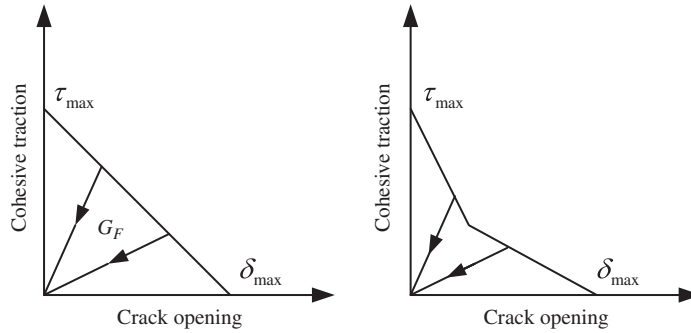


Figure 9. Linear and bilinear cohesive law; the area under the cohesive law curve is the same as the fracture energy  $G_F$ .

used for small displacement problems, so the constitutive relation is given as

$$\sigma_{ij} = (1 - D)C_{ijkl}\epsilon_{kl} \tag{51}$$

where  $D$  can have values from 0 to 1,  $C_{ijkl}$  is the elastic modulus of the undamaged material, and  $\sigma_{ij}$  and  $\epsilon_{kl}$  are Cauchy stress and linear strain components, respectively. As can be seen from Equation (51), an increase in damage parameter  $D$  leads to a softer material response. The damage evolution law is given by

$$D(\bar{\epsilon}) = 1 - (1 - A)\epsilon_{D_0}\bar{\epsilon}^{-1} - Ae^{-B(\bar{\epsilon}-\epsilon_{D_0})} \tag{52}$$

where  $\bar{\epsilon}$  is the effective strain,  $A$  and  $B$  are material parameters and  $\epsilon_{D_0}$  is the strain threshold. The effective strain  $\bar{\epsilon}$  is defined as

$$\bar{\epsilon} = \sqrt{\sum_{i=1}^3 \langle \epsilon_i \rangle^2} \tag{53}$$

where  $\epsilon_i$  is the  $i$ th principal strain and  $\langle \cdot \rangle$  is the Macaulay bracket. Note that in Equation (53), the compressive strain components are filtered out by the Macaulay bracket, and therefore do not contribute to the damage.

### 4.3. Thermo-elasto-viscoplastic model

For shear band simulations, we used a thermo-elasto-viscoplastic constitutive model in which heat conduction is neglected for simplicity. The rate form of the constitutive equation is given by

$$\overset{\nabla}{\boldsymbol{\tau}} = \mathbf{C}^{\text{elas}} : (\mathbf{D} - \mathbf{D}^{\text{vp}} - \mathbf{D}^t) \tag{54}$$

where,  $\overset{\nabla}{\boldsymbol{\tau}}$  is the Jaumann rate of Kirchhoff stress,  $\mathbf{C}^{\text{elas}}$  is the elastic moduli tensor,  $\mathbf{D}^{\text{vp}}$  is the viscoplastic rate of deformation and  $\mathbf{D}^t$  is the thermal rate of deformation. For the von-Mises material with isotropic hardening condition, the viscoplastic rate of deformation,  $\mathbf{D}^{\text{vp}}$ ,

is given by

$$\mathbf{D}^{\text{vp}} = \frac{3\dot{\bar{\epsilon}}}{2\bar{\sigma}} \boldsymbol{\tau}' \quad (55)$$

where,  $\boldsymbol{\tau}'$  is the deviatoric part of Kirchhoff stress and  $\bar{\sigma}$  is the effective stress.  $\dot{\bar{\epsilon}}$  is the effective plastic strain rate which is characterized by the power law relation of

$$\dot{\bar{\epsilon}} = \dot{\epsilon}_0 \left[ \frac{\bar{\sigma}}{g(\bar{\epsilon}, T)} \right]^m \quad (56)$$

where  $m$  is a power index, which indicates the rate sensitivity of the material and  $g(\bar{\epsilon}, T)$  is the material hardening or softening parameter. In this study  $g(\bar{\epsilon}, T)$  is given by

$$g(\bar{\epsilon}, T) = \sigma_0 \left[ 1 + \frac{\bar{\epsilon}}{\epsilon_0} \right]^N \left\{ 1 - \delta \left[ \exp \left( \frac{T - T_0}{k} \right) - 1 \right] \right\} \quad (57)$$

The details about the constitutive equation can be found in References [21–24]. The thermal rate of deformation,  $\mathbf{D}^t$ , is given as

$$\mathbf{D}^t = \alpha \dot{T} \mathbf{I} \quad (58)$$

where  $\alpha$  is thermal expansion coefficient. For adiabatic heating, we have

$$\rho_0 C_p \dot{T} = \chi \boldsymbol{\tau} : \mathbf{D}^{\text{vp}} \quad (59)$$

where  $\chi$  is the fraction of plastic work converted to heat. For the explicit stress update algorithm, we employed the rate tangent modulus algorithm given by Peirce *et al.* [25].

#### 4.4. Continuum to discontinuity transition

The discontinuous crack or shear band model is initiated when the material loses stability. In rate-independent materials, loss of stability coincides with loss of hyperbolicity and the conditions are well known; for examples, see Reference [1].

In a rate-dependent material, hyperbolicity is not lost, so the transition to a discontinuity is governed by material instability. Material instability can be determined as usual by examining whether growth occurs in an initially stressed infinite body perturbed by (see, Reference [17, p. 386])

$$\tilde{\mathbf{u}} = \mathbf{h}_1 \cdot \mathbf{e}^{\text{at}} \cdot \mathbf{e}^{i(bt + k\mathbf{h}_2 \cdot \mathbf{X})} \quad (60)$$

where  $\mathbf{h}_1$  is the polarization direction,  $\mathbf{h}_2$  is the direction of the wave,  $k$  is the wave number and  $a$  is a real number that determines the stability of the response; if  $a > 0$  the response is unstable. The conditions that  $a > 0$  coincides with the condition that there exist  $\mathbf{h}_1$  and  $\mathbf{h}_2$  such that

$$\mathbf{h}_1 \otimes \mathbf{h}_2 : \mathbf{A} : \mathbf{h}_1 \otimes \mathbf{h}_2 < 0 \quad \forall \mathbf{h}_i \quad (61)$$

where  $\mathbf{A}$  relates the rate of stress to the rate of strain. At the point that  $\mathbf{h}_i$  are found such that Equation (61) holds, a discontinuity is introduced such that  $\nabla \mathbf{f}$  is parallel to  $\mathbf{h}_2$ . A detailed analysis is given in Reference [26].

## 5. NUMERICAL EXAMPLES

## 5.1. Edge-cracked plate under impulsive loading

5.1.1. *Problem description.* These simulations concern an experiment reported by Kalthoff and Winkler [27] in which a plate with two initial edge notches is impacted by a projectile. The experiment is shown in Figure 10. In the experiment, two different failure modes were observed by modifying the projectile speed,  $v_0$ ; at high impact velocities, a shear band is observed to emanate from the notch at an angle of  $-10^\circ$  with respect to initial notch; at lower strain rates, brittle failure with a crack propagation angle of about  $70^\circ$  is observed. In this study, we consider both failure modes.

To take advantage of the twofold symmetry of the configuration, only the upper half of the plate is modelled: at the bottom edge of the finite element model,  $u_y = 0$  and  $t_x = 0$ . The initial impact velocity is applied on the left edge on the segment  $0 \leq y \leq 25$  mm. We assumed that the projectile has the same elastic impedance as the specimen, so we applied one half of the projectile speed, 16.5 m/s for the brittle fracture mode and 32.0 m/s for the shear

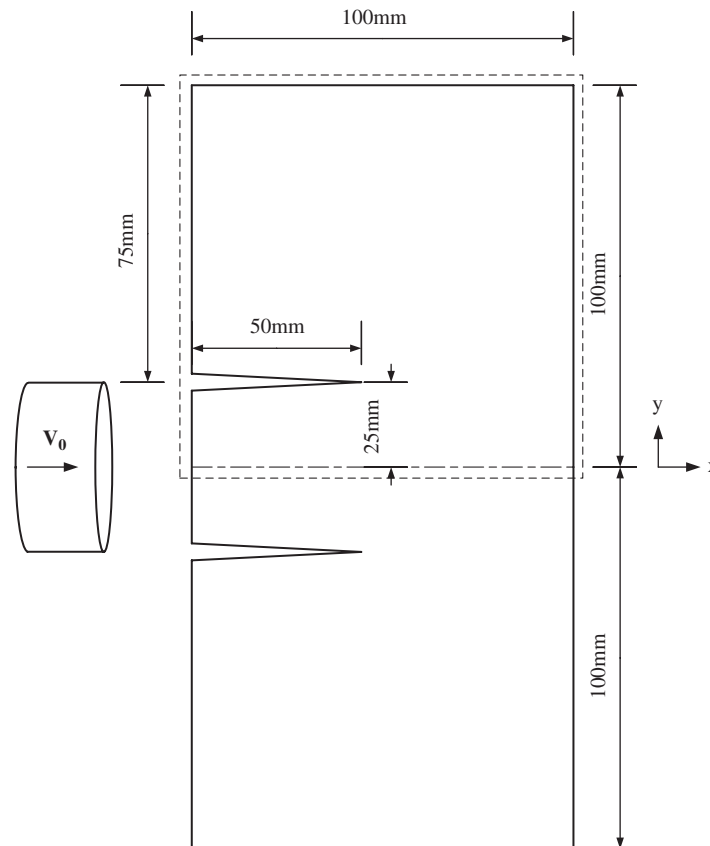


Figure 10. Experimental set-up for edge-cracked plate under impulsive loading: dash line denotes the numerically modelled region.

mode, to the left edge as an initial condition (see, References [28, 29]). The initial notch was modelled by including two lines of nodes separated by 0.3 mm. The material is a maraging steel 18Ni1900 [30] and its material properties are  $\rho = 8000 \text{ kg/m}^3$ ,  $E = 190 \text{ GPa}$  and  $\nu = 0.30$ . The initial Rayleigh wave speed is  $c_R = 2799.2 \text{ m/s}$ . We used a central difference time integration scheme with a Courant number of 0.1. We found that a low Courant number is necessary for the elements which contain a discontinuity.

*5.1.2. Dynamic crack propagation with a damage model.* We considered a Lemaitre damage constitutive model [31], Equation (51) with  $A = 1.0$ ,  $B = 200.0$  and  $\varepsilon_{D_0} = 3.0 \times 10^{-3}$ . A cohesive crack model with fracture energy  $G_F = 2.213 \times 10^4 \text{ N/m}$  and  $\delta_{\max} = 5.245 \times 10^{-5} \text{ m}$  in Equation (50) and a linear cohesive law was used. For the crack initiation criterion, we used the maximum tensile stress criterion. The stresses around crack tip were smoothed by a moving least square projection. Numerical simulations were made with two different meshes to observe mesh sensitivity:  $50 \times 50$  and  $100 \times 100$  meshes.

The results for the  $100 \times 100$  mesh and comparison of  $50 \times 50$  and  $100 \times 100$  meshes are shown in Figures 11 and 12, respectively. Both simulations are concluded at around  $80 \mu\text{s}$

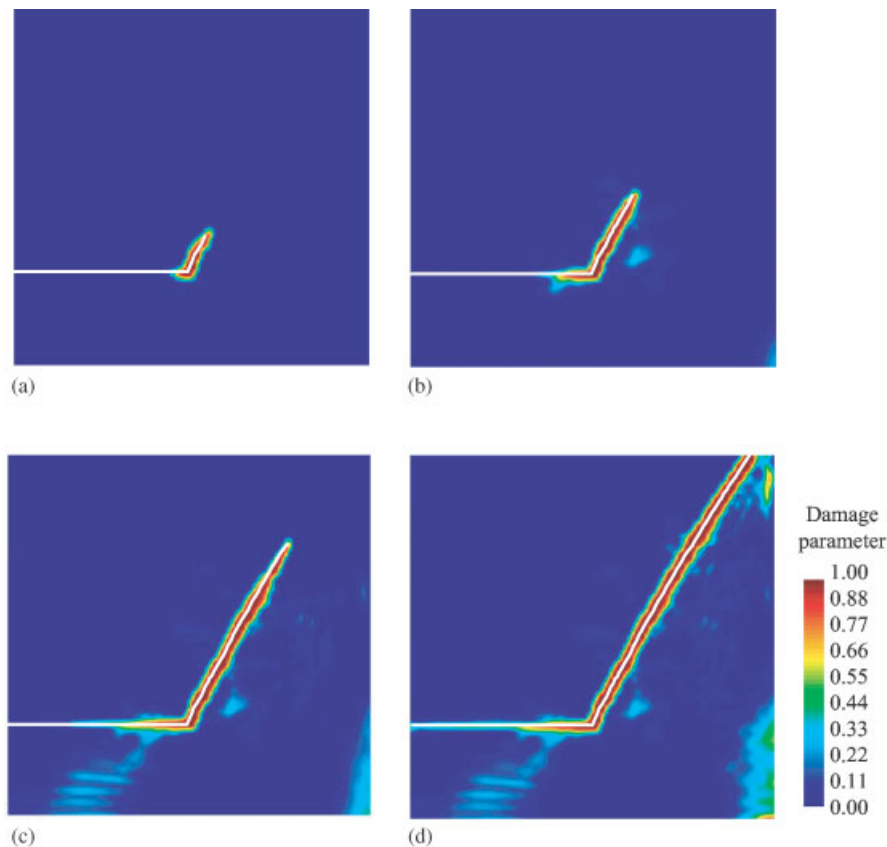


Figure 11. The crack path for a  $100 \times 100$  quadrilateral mesh with a Lemaitre damage model at different time steps: (a)  $t = 39.29 \mu\text{s}$ ; (b)  $t = 42.86 \mu\text{s}$ ; (c)  $t = 53.58 \mu\text{s}$ ; and (d)  $t = 88.58 \mu\text{s}$ .

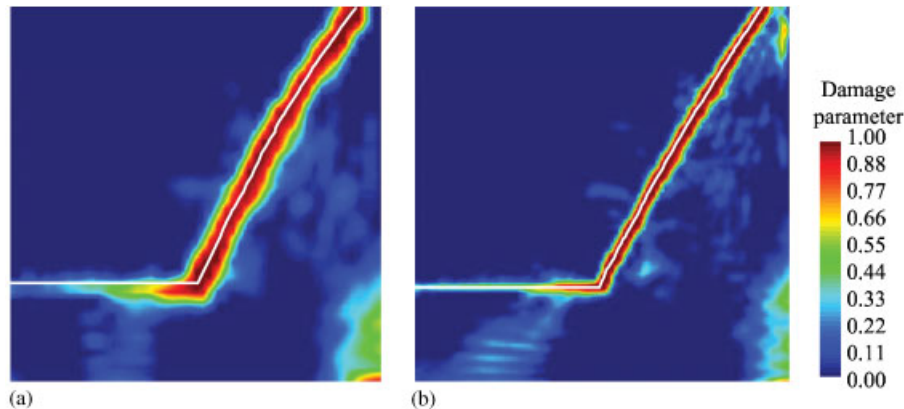


Figure 12. Comparison of crack path for  $50 \times 50$  and  $100 \times 100$  quadrilateral meshes with a Lemaitre damage model at  $t = 88.58 \mu\text{s}$ : (a)  $50 \times 50$  quadrilateral mesh; and (b)  $100 \times 100$  quadrilateral mesh.

when the crack tip reaches the upper boundary. Both results show very similar trajectories for the crack. The initial crack propagation angle is around  $64^\circ$  and the average angle from the initial crack tip to the final crack tip is about  $60^\circ$  for both meshes; the crack path is nearly straight. This angle is  $10^\circ$  smaller than the observed angle [27] and the angle obtained by mesh-free computations in References [11, 32, 33]. In the latter, the crack tip singularity was included as an enrichment at the notch. Evidently, due to approximation errors of constant strain elements, the near-tip field is not reproduced well enough to yield an accurate direction for crack propagation. However, for most engineering purposes, the accuracy is more than adequate. There are damaged areas in the bottom right corner of the model due to wave reflection.

The crack tip propagation speed is shown in Figure 13. The crack tip speed never exceeds the Rayleigh wave speed  $2799.2 \text{ m/s}$ . For the  $50 \times 50$  mesh, the crack tip speed is substantially higher than reported in Belytschko *et al.* [1] for a  $80 \times 80$  cross-triangular mesh with the method that modelled crack progression within the element. This suggests that element-by-element propagation of the crack introduces some errors in crack tip speed for coarse meshes, and in particular, it appears to increase the predicted crack tip speed. However, the crack tip speed for the  $100 \times 100$  mesh decreases and agrees better with the computation of Belytschko *et al.* [1]. Note that the crack tip speed is taken to be the average over five time steps.

**5.1.3. Dynamic crack and shear band propagation with a elasto-viscoplastic model.** In this example, we simulate both brittle and shear fracture mode of Kalthoff and Winkler experiment [27]. To observe dynamic shear band propagation, we employed a thermo-elasto-viscoplastic constitutive model [22–24] with an explicit stress update algorithm [25]. The material is a maraging steel, 18Ni1900, as in the preceding example and the material properties for the thermo-elasto-viscoplastic constitutive model can be found in References [23, 24]. For the crack and shear band criterion, as an indicator of the propagation and the direction, the maximum tensile stress and loss of material stability condition, respectively, are employed. Note that an elasto-viscoplastic constitutive model does not lose hyperbolicity.

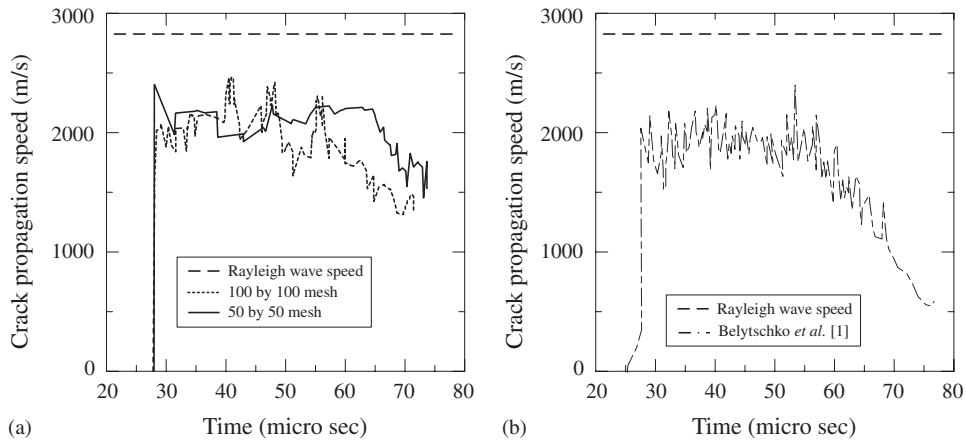


Figure 13. Crack tip propagation speed for the edge-cracked plate under impulsive loading: (a) the crack tip propagation speed of this method and (b) the crack tip propagation speed of the previous results in Reference [1], where a  $80 \times 80$  cross-triangular mesh is used.

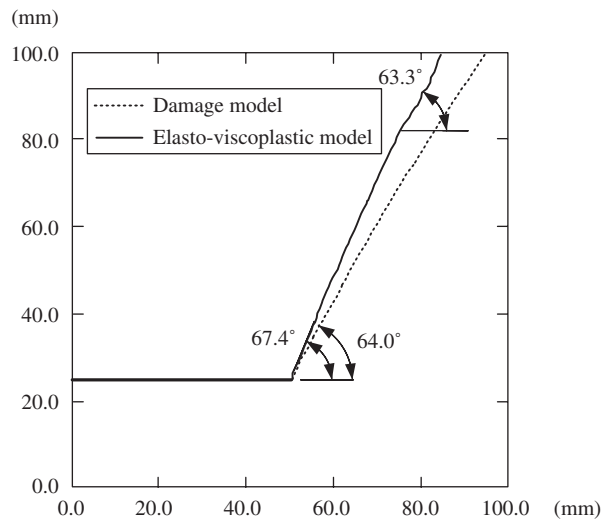


Figure 14. The comparison of crack growth path between the simulation with the damage model and the elasto-viscoplastic model.

At 16.5 m/s as in the preceding example, we observe dynamic crack propagation. The comparison of the crack growth paths between the results with damage model and elasto-viscoplastic model are shown in Figure 14. The crack growth paths of the elasto-viscoplastic model agree better with the experimental results than those for the hypo-elastic constitutive law with damage. The initial crack propagation angle is around  $67.4^\circ$  and the average overall

crack propagation angle is  $65.1^\circ$ . This  $2\text{--}5^\circ$  discrepancy in the angle with the experiment may be due to the absence of a crack tip stress concentration. At the end of crack propagation, we can observe some minor oscillations in the crack path because of a reduced moving least square projection domain.

At 32 m/s, the effective plastic strain distribution and a comparison of the shear band path with experimental results are shown in Figure 15. We assumed that the shear band energy is  $G_F = 1.0 \times 10^2 \text{ N/m}$ . In this study, since we adopted a strong discontinuity approach to represent sheared elements, the localized plastic strain along the shear band is substantially lower than that of the physical shear band. However, as we can observe from Figure 15(b), the overall shear band propagation path agrees quite well with the experimental results [29], though the shear band path drifted downward more than the experimental results along the last half of the path.

### 5.2. Crack branching

In this example, we consider a prenotched specimen  $0.1 \text{ m} \times 0.04 \text{ m}$  as shown in Figure 16. Tensile tractions,  $\sigma = 1 \text{ MPa}$ , are applied on the both of the top and the bottom edges as a step function in time. Numerical results for this problem have been given by Belytschko *et al.* [1], Rabczuk and Belytschko [8], Xu and Needleman [9] and experimental results with different dimensions are available in References [34–38].

We used the Lemaitre damage law [31] for the continuum domain and imposed a linear cohesive law once a discontinuity developed. The material properties are  $\rho = 2450 \text{ kg/m}^3$ ,  $E = 32 \text{ GPa}$  and  $\nu = 0.20$ . We used  $A = 1.0$ ,  $B = 7300.0$  and  $\varepsilon_{D0} = 8.5 \times 10^{-5}$  for the Lemaitre damage model [31]. The initial Rayleigh wave speed is  $c_R = 2119.0 \text{ m/s}$ . For the discretization, we modelled the domain with  $100 \times 51$  uniform quadrilateral elements and used explicit time integration with a Courant number of 0.1.

To capture the crack branching phenomena, we monitored the maximum principal stress criterion at several points around the crack tip. If this criterion is satisfied and the

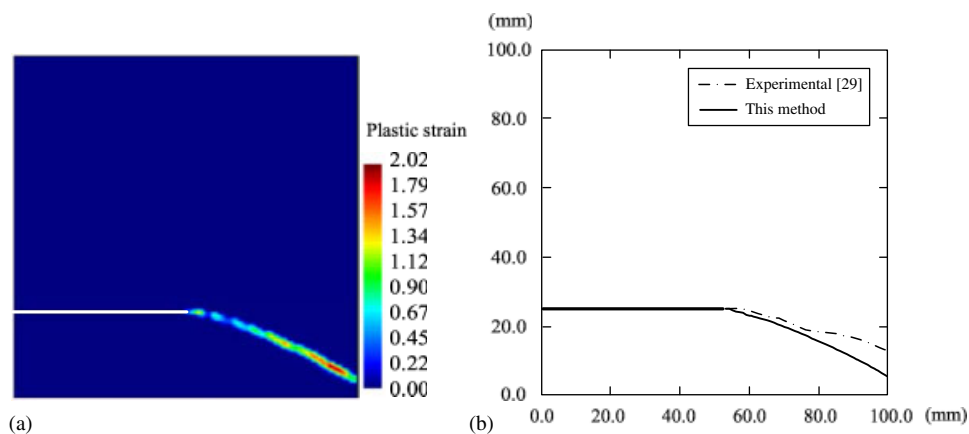


Figure 15. Dynamic shear band propagation: (a) effective plastic strain distribution at  $t = 35.00 \mu\text{s}$ ; and (b) comparison of shear band path with experimental results [29].

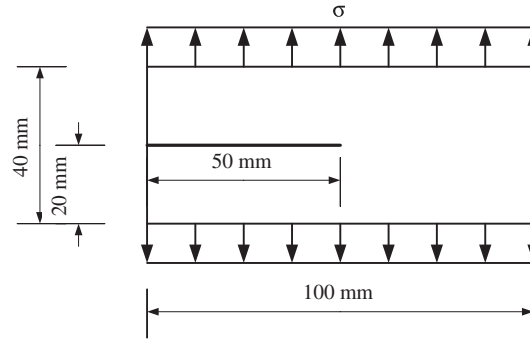


Figure 16. Plate with a horizontal initial notch under tensile stress.

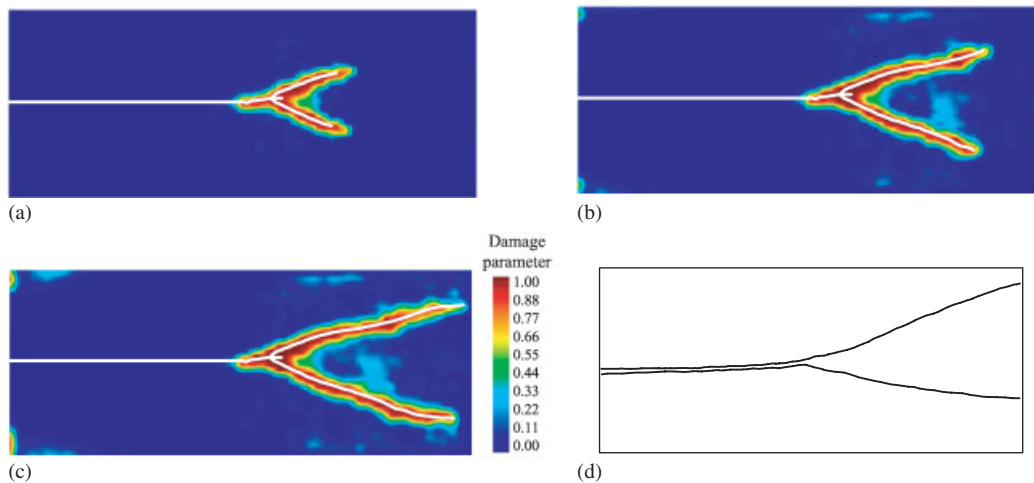


Figure 17. Crack branching and damage evolution at different time steps: (a)  $t = 30.29 \mu\text{s}$ ; (b)  $t = 46.14 \mu\text{s}$ ; (c)  $t = 55.93 \mu\text{s}$ ; and (d) a sketch of the experiment paths reported by Ramulu and Kobayashi [34].

maximum principal stress directions show relatively different crack growth angles, we initiate crack branches. For simplicity, we only allow the crack to branch once and set the element stress to zero in elements in which three cracks have formed. The pattern of crack propagation is shown in Figure 17(a–c) and the crack tip speed is shown in Figure 18. The crack begins to propagate at  $15.38 \mu\text{s}$ . From this initial phase until crack branching, the crack tip speed increases linearly and peaks at around  $20.04 \mu\text{s}$ ; at this point the crack branches into two cracks. After branching, the crack tip speed becomes almost constant at 75% of the Rayleigh wave speed. This agrees with the results, which were reported by Belytschko *et al.* [1], and Rabczuk and Belytschko [8]. The numerical simulation finishes at  $55.93 \mu\text{s}$  when the crack tip reaches the boundary of the specimen. The crack pattern is similar to the experimental results reported in References [34–38].

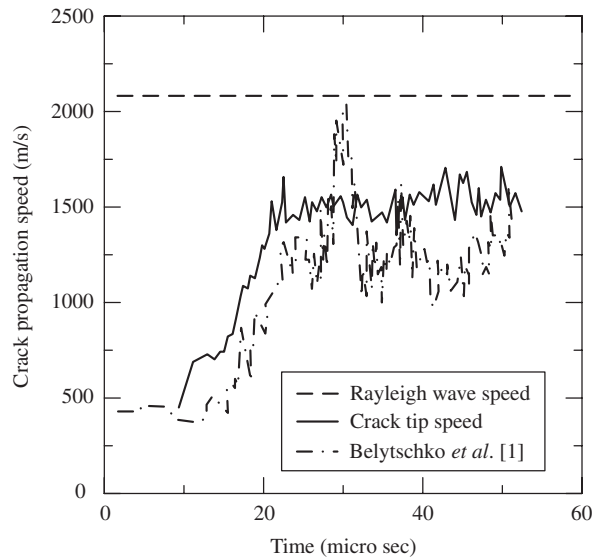


Figure 18. Crack propagation speed for the crack branching problem compared to [1].

### 5.3. Mixed mode crack propagation in a beam under impact loading

An experimental study of mixed mode dynamic crack propagation in concrete beams has been reported by John and Shah [39]. The experimental configuration is shown in Figure 19(a). In the experiment, the pattern of crack propagation depends mainly on the location of initial notch. The location of notch is characterized by the offset parameter  $\gamma$ .

$$\gamma = \frac{d_{\text{notch}}}{L/2} \quad (62)$$

where  $d_{\text{notch}}$  denotes the distance between the midspan and the notch, and  $L$  is the span between the supports. For  $\gamma=0$ , John and Shah [39] reported pure mode I fracture, while  $\gamma > 0$  can result in either a mode I fracture at the midspan or a mixed mode fracture at the offset notch; see, Figure 19(b–d). Numerical simulations of this experiment by the mesh-free methods have been reported by Belytschko and Tabbara [33].

Simulations were conducted with various offset parameters to examine the different crack growth trajectories according to  $\gamma$ . We discretized the  $0.2286 \text{ m} \times 0.0762 \text{ m}$  concrete beam with a  $30 \times 91$  mesh and used the following material properties:  $\rho = 2400 \text{ kg/m}^3$ ,  $E = 31.37 \text{ GPa}$ ,  $\nu = 0.20$ ;  $A = 1.0$ ,  $B = 7300.0$  and  $\varepsilon_{D_0} = 8.5 \times 10^{-5}$  for the Lemaitre damage model in Equation (52). To represent an impact loading, we used a ramp loading instead of a direct impact loading because of a rubber pad which is located between the beam and impact hammer (for more details, refer to References [33, 39]). For the simulation of the midspan crack growth, we allow a crack to initiate at the midspan. Note that the finite element model has only one physical notch at the initial stage of the simulations.

As we can see from Figure 20(a) for  $\gamma=0.7$ , the crack propagates only from the offset notch since the stress is released at the midspan. In this case, the crack propagates at an angle of  $52^\circ$ , which is in reasonable agreement with the experimental result of  $60^\circ$ . For the offset

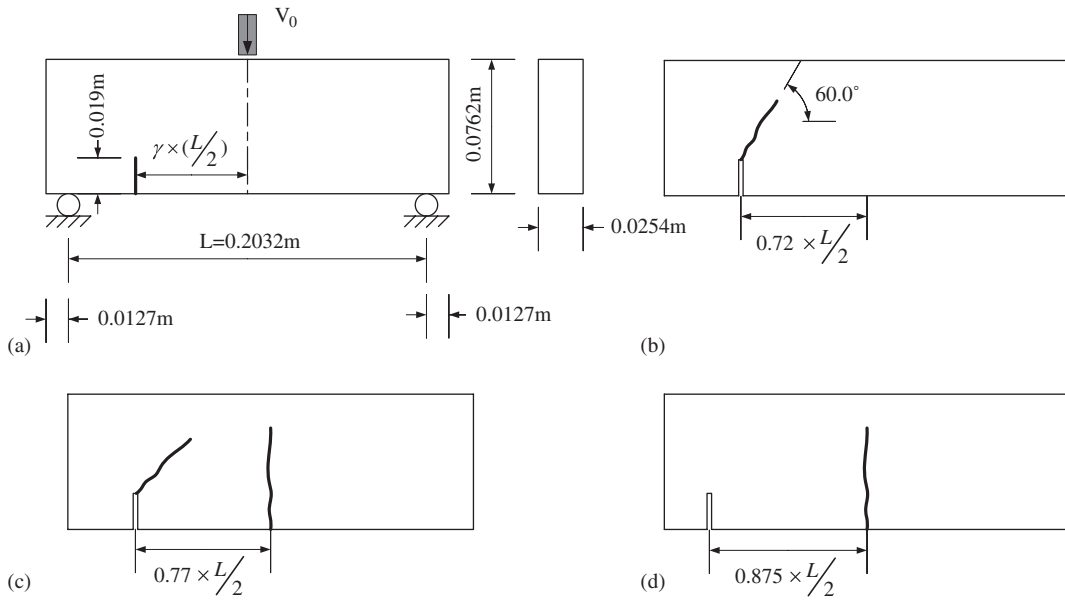


Figure 19. Test configuration of concrete beam with an offset notch for a mixed mode test and experiment crack configurations for various offset parameters,  $\gamma$  [39]: (a) experiment set-up; (b) mixed mode fracture at the initial notch; (c) transition stage; and (d) mode I fracture at the midspan.

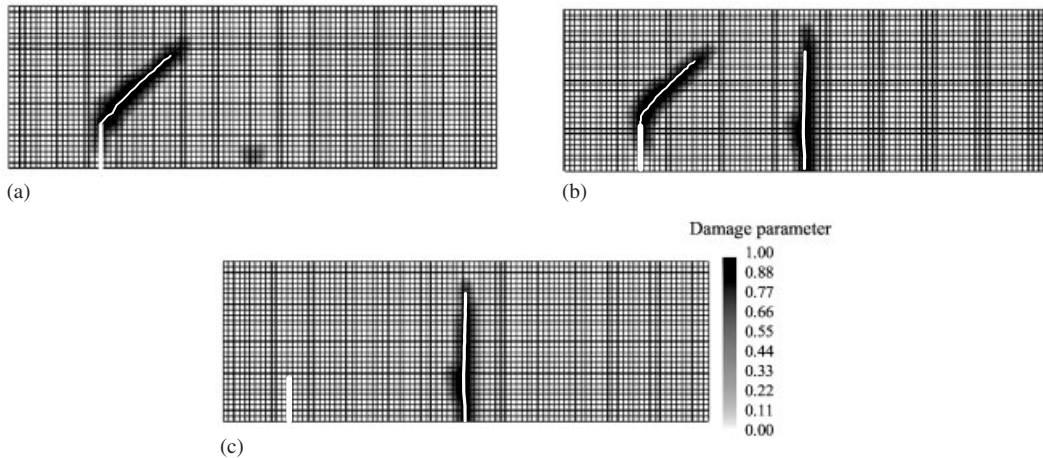


Figure 20. Final crack growth path with damage evolution for different offset parameter  $\gamma$ : (a)  $\gamma = 0.7$ ; (b)  $\gamma = 0.75$ ; and (c)  $\gamma = 0.8$ .

notch in the transition zone (i.e.  $\gamma = 0.77$ ), the crack is initiated at the midspan and both cracks propagate simultaneously. In this simulation, the transition is observed around  $\gamma = 0.75$ , which is similar to that observed experimentally. Finally, when the offset notch is too far from the

loading point and it cannot relax the stress at the midspan, the crack is initiated at the bottom of the midspan and grows as shown in Figure 20(c). For all cases, the crack starts to grow at around 620  $\mu\text{s}$ .

## 6. CONCLUSIONS

A method for explicit dynamic crack and shear band propagation simulation has been developed. In this method, by reinterpreting the conventional XFEM displacement field, a cracked or sheared element is represented by two superimposed elements with a set of phantom nodes or phantom degrees of freedom. The numerical integration of the cracked elements is simplified with one-point quadrature and hourglass control. This facilitates the addition of this method to existing programs.

To evaluate the applicability of the proposed method, several numerical examples for which experimental or numerical results are available have been analysed. In the Kalthoff and Winkler problem, the method showed a little mesh dependence. However, the crack tip speed decreases somewhat with mesh size. We attribute this effect to the element-by-element cracking procedure, i.e. due to the absence of a model for a partially cracked element. It is apparent that element-by-element cracking requires finer meshes to match the accuracy of methods with partial element cracking as in [1]. So while element-by-element progression of a crack is simple, it tends to overestimate the crack speed. Overall crack and shear band propagation paths are in reasonable agreement with what was obtained experimentally. In the dynamic crack branching problem, we found that the proposed method is quite effective for these complicated crack patterns.

An attractive feature of this method is that it provides consistent history variables and low computational cost within the context of the conventional explicit finite element method. This allows large-scale problems with complicated crack geometries to be solved efficiently.

## ACKNOWLEDGEMENTS

The support of the Office of Naval Research under award N0001H-98-1-0578 is gratefully acknowledged.

## REFERENCES

1. Belytschko T, Chen H, Xu J, Zi G. Dynamic crack propagation based on loss of hyperbolicity with a new discontinuous enrichment. *International Journal for Numerical Methods in Engineering* 2003; **58**:1873–1905.
2. Hansbo A, Hansbo P. A finite element method for the simulation of strong and weak discontinuities in solid mechanics. *Computer Methods in Applied Mechanics and Engineering* 2004; **193**:3523–3540.
3. Belytschko T, Black T. Elastic crack growth in finite elements with minimal remeshing. *International Journal for Numerical Methods in Engineering* 1999; **45**(5):601–620.
4. Moës N, Dolbow J, Belytschko T. A finite element method for crack growth without remeshing. *International Journal for Numerical Methods in Engineering* 1999; **46**(1):131–150.
5. Babuška I, Banerjee U, Osborne JE. On the principles for the selection of shape functions for the generalized finite element methods. *Computer Methods in Applied Mechanics and Engineering* 2002; **191**:5595–5629.
6. Chessa J, Wang H, Belytschko T. On the construction of blending elements for local partition of unity enriched finite elements. *International Journal for Numerical Methods in Engineering* 2003; **57**(7):1015–1038.
7. Ventura G, Xu JX, Belytschko T. A vector level set method and new discontinuity approximations for crack growth by EFG. *International Journal for Numerical Methods in Engineering* 2002; **54**(6):923–944.

8. Rabczuk T, Belytschko T. Cracking particles: a simplified meshfree method for arbitrary evolving cracks. *International Journal for Numerical Methods in Engineering* 2004; **61**(13):2316–2343.
9. Xu X-P, Needleman A. Numerical simulation of fast crack growth in brittle solids. *Journal of Mechanics and Physics of Solids* 1994; **42**(9):1397–1434.
10. Ortiz M, Pandolfi A. A class of cohesive elements for the simulation of three-dimensional crack propagation. *International Journal for Numerical Methods in Engineering* 1999; **44**:1267–1282.
11. Réthoré J, Gravouil A, Combescure A. An energy-conserving scheme for dynamic crack growth using the extended finite element method. *International Journal for Numerical Methods in Engineering* 2005; **63**:631–659.
12. Areias PMA, Belytschko T. Analysis of three-dimensional crack initiation and propagation using the extended finite element method. *International Journal for Numerical Methods in Engineering* 2005; **63**:760–788.
13. Mergheim J, Kuhl E, Steinmann P. A finite element method for the computational modelling of cohesive cracks. *International Journal for Numerical Methods in Engineering* 2005; **63**:276–289.
14. Stolarska M, Chopp DL, Moës N, Belytschko T. Modeling crack growth by level sets in the extended finite element method. *International Journal for Numerical Methods in Engineering* 2001; **51**(8):943–960.
15. Belytschko T, Moës N, Usui S, Parimi C. Arbitrary discontinuities in finite elements. *International Journal for Numerical Methods in Engineering* 2001; **50**(4):993–1013.
16. Areias PMA, Belytschko T. A comment on the article: a finite element method for simulation of strong and weak discontinuities in solid mechanics. *Computer Methods in Applied Mechanics and Engineering* 2005, in press.
17. Belytschko T, Liu WK, Moran B. *Nonlinear Finite Elements for Continua and Structures*. Wiley: New York, 2000.
18. Flanagan DP, Belytschko T. A uniform strain hexahedron and quadrilateral and orthogonal hourglass control. *International Journal for Numerical Methods in Engineering* 1981; **17**:679–706.
19. Daniel WJT, Belytschko T. Suppression of spurious intermediate frequency modes in under-integrated elements by combined stiffness/viscous stabilization. *International Journal for Numerical Methods in Engineering* 2005; **64**:335–353.
20. Lemaitre J, Chaboche JL. *Mechanics of Solid Materials*. Cambridge University Press: Cambridge, 1990. ISBN 0 521 32853 5.
21. Perzyna P. *Thermodynamic Theory of Viscoplasticity*. Academic Press: New York, 1971.
22. Lemonds J, Needleman A. Finite element analyses of shear localization in rate and temperature dependent solids. *Mechanics of Materials* 1986; **5**:339–361.
23. Zhou M, Ravichandran G, Rosakis AJ. Dynamically propagating shear bands in impact-loaded prenotched plates-ii. Numerical simulations. *Journal of the Mechanics and Physics of Solids* 1996; **44**:1007–1032.
24. Li S, Liu WK, Rosakis AJ, Belytschko T, Hao W. Meshfree Galerkin simulations of dynamic shear band propagation and failure mode transition. *International Journal of Solids and Structures* 2002; **39**:1213–1240.
25. Peirce D, Shih CF, Needleman A. A tangent modulus method for rate dependent solids. *Computers and Structures* 1984; **18**:875–887.
26. Belytschko T, Song J-H. Stability of rate dependent materials, submitted.
27. Kalthoff JF, Winkler S. Failure mode transition at high rates of shear loading. *International Conference on Impact Loading and Dynamic Behavior of Materials* 1987; **1**:185–195.
28. Lee YJ, Freund LB. Fracture initiation due to asymmetric impact loading of an edge cracked plate. *Journal of Applied Mechanics* (ASME) 1990; **57**:104–111.
29. Kalthoff JF. Modes of dynamic shear failure in solids. *International Journal of Fracture* 2000; **101**:1–31.
30. Decker RF. *Source Book on Maraging Steels*. American Society for Metals, 1979.
31. Lemaitre J. Evaluation of dissipation and damage in metal submitted to dynamic loading. *Proceedings ICM 1*, 1971.
32. Belytschko T, Lu YY, Gu L, Tabbara M. Element-free Galerkin methods for static and dynamic fracture. *International Journal of Solids and Structures* 1995; **32**:2547–2570.
33. Belytschko T, Tabbara M. Dynamic fracture using element-free Galerkin methods. *International Journal for Numerical Methods in Engineering* 1996; **39**:923–938.
34. Ramulu M, Kobayashi AS. Mechanics of crack curving and branching—a dynamic fracture analysis. *International Journal of Fracture* 1985; **27**:187–201.
35. Ravi-Chandar K. Dynamic fracture of nominally brittle materials. *International Journal of Fracture* 1998; **90**:83–102.

36. Sharon E, Gross PSP, Fineberg J. Local crack branching as a mechanism for instability in dynamic fracture. *Physical Review Letters* 1995; **74**(25):5096–5099.
37. Sharon E, Fineberg J. Microbranching instability and the dynamic fracture of brittle materials. *Physical Review B* 1996; **54**(10):7128–7139.
38. Fineberg J, Sharon E, Cohen G. Crack front waves in dynamic fracture. *International Journal of Fracture* 2003; **121**(1–2):55–69.
39. John R, Shah SP. Mixed mode fracture of concrete subjected to impact loading. *Journal of Structural Engineering* (ASCE) 1988; **116**:585–602.